Ebullition and storm-induced methane release from the East Siberian Arctic Shelf

Natalia Shakhova[1,2]*†, Igor Semiletov[1,2]†, Ira Leifer[3,4]†, Valentin Sergienko[5], Anatoly Salyuk[2], Denis Kosmach[2], Denis Chernykh[2], Chris Stubbs[3], Dmitry Nicolsky[6], Vladimir Tumskoy[7] and Örjan Gustafsson[8]

Vast quantities of carbon are stored in shallow Arctic reservoirs, such as submarine and terrestrial permafrost. Submarine permafrost on the East Siberian Arctic Shelf started warming in the early Holocene, several thousand years ago. However, the present state of the permafrost in this region is uncertain. Here, we present data on the temperature of submarine permafrost on the East Siberian Arctic Shelf using measurements collected from a sediment core, together with sonar-derived observations of bubble flux and measurements of seawater methane levels taken from the same region. The temperature of the sediment core ranged from −1.8 to 0 °C. Although the surface layer exhibited the lowest temperatures, it was entirely unfrozen, owing to significant concentrations of salt. On the basis of the sonar data, we estimate that bubbles escaping the partially thawed permafrost inject 100–630 mg methane m^{-2} d^{-1} into the overlying water column. We further show that water-column methane levels had dropped significantly following the passage of two storms. We suggest that significant quantities of methane are escaping the East Siberian Shelf as a result of the degradation of submarine permafrost over thousands of years. We suggest that bubbles and storms facilitate the flux of this methane to the overlying ocean and atmosphere, respectively.

The vast reduced-carbon pool sequestered in shallow Arctic reservoirs could alter atmospheric greenhouse gas budgets significantly if remobilized from terrestrial and marine systems to the atmosphere on decadal/centennial timescales[1–4]. Among Arctic reservoirs, subsea permafrost, hydrates, and associated CH$_4$ deposits are the most worrisome owing to high heat transfer from rapidly warming shallow Arctic seas[5–9]. In the East Siberian Arctic Shelf (ESAS), which comprises ∼25% of the Arctic shelf, subsea permafrost warming started in the early Holocene when this shelf was inundated by sea water[10,11]. As the mean temperatures of ESAS bottom water vary from slightly below to slightly above 0 °C, approaching equilibrium means that subsea permafrost is also approaching the thaw point.

Nevertheless, knowledge about the present thermal state of subsea permafrost is mainly based on modelling results, which are controversial[11–15]. Some authors suggest that it would take ∼5–7 thousand years for subsea permafrost to reach the thaw point[11]. Others believe that in the coastal areas, where permafrost was submerged most recently, taliks (that is, layers or columns of thawed sediments within permafrost) might form as the result of the combined effect of geothermal flux from fault zones, the warming effect of rivers, and the already-present thermokarst[12,13,16]. Destabilization of subsea permafrost results in increasing permeability for gaseous CH$_4$ long preserved in seabed deposits within and beneath permafrost[6,10]. This process manifests as extensive CH$_4$ ebullition, driving significantly elevated CH$_4$ aqueous concentrations to a factor of 10^3 above atmospheric equilibrium[5].

In the marine environment, some bubbles escaping the seabed dissolve into the water column, whereas some directly transport CH$_4$ to the atmosphere leaving almost no traces in the water column[17]. The partitioning depends on specific characteristics of the bubbles (bubble size, rise velocity, release intensity) and properties of the environment (water depth, temperature, salinity, stratification, sediment qualities)[17,18]. Upwelling flow due to massive occurrence of rising bubbles can increase bubble rise velocity by up to 2 m s^{-1}, shortening the residence time of bubbles in the water column markedly[19,20]. The upwelling flow decreases bubbles' sub-surface residence time, diminishes dissolution, and significantly enhances CH$_4$ transport to the atmosphere[17,19]. Upwelling flow lifts colder and more saline water up to the surface; it also displaces and lifts sediment particles, which causes disturbance of the sulphate-reduction zone where sedimentary CH$_4$ is usually anaerobically oxidized[21].

In the ESAS, where the mean water-column depth is <50 m, bubble residence time in the water column could be minimized to seconds. Ebullition could, therefore, be a very important contributor to atmospheric CH$_4$ emissions in the ESAS. Nevertheless, quantifying bubble-induced CH$_4$ fluxes is highly challenging. Active sonar observations have been used to observe bubble-induced emissions in non-Arctic environments[22–24], but quantitative derivation of bubble fluxes for other than individual spherical bubbles remains difficult because seeps generally occur as large bubble plumes. Moreover, a number of factors affect the seabed, water-column, and sea–air fluxes[18–20].

[1]International Arctic Research Center, University of Alaska, Akasofu Building, Fairbanks, Alaska 99775-7320, USA, [2]Russian Academy of Sciences, Far Eastern Branch, Pacific Oceanological Institute, 43 Baltiiskaya Street, Vladivostok 690041, Russia, [3]Marine Sciences Institute, University of California, Santa Barbara, California 93106, USA, [4]Bubbleology Research International, Solvang, California 93463, USA, [5]Russian Academy of Sciences, Far Eastern Branch, Institute of Chemistry, 159, 100-Let Vladivostok Prospect, Vladivostok 690022, Russia, [6]Geophysical Institute, University of Alaska, 903 Koyukuk Drive, Fairbanks, Alaska 99775-7320, USA, [7]Moscow State University, 1-12 Leninskie Gory, Moscow, Moscow 119991, Russia, [8]Department of Applied Environmental Science and Bolin Centre for Climate Research, Stockholm University, Stockholm 10691, Sweden. †These authors contributed equally to this work. *e-mail: nshakhov@iarc.uaf.edu
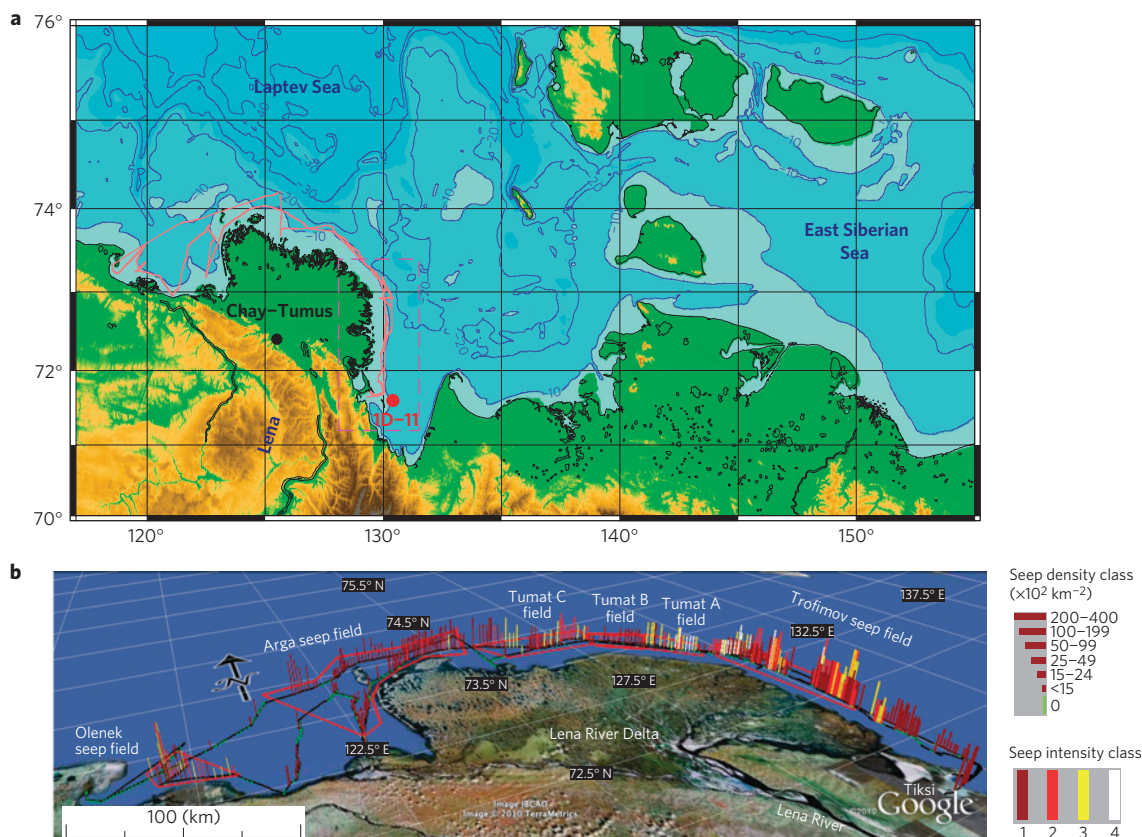
Figure 1 | Study area. a, ESAS bathymetric map (water depths ≤ 50 m). The location of the study area is marked with the dotted pink rectangle. The red freeform line shows the ship track followed for the multibeam survey referred to in **b**. The black circle shows the position of the borehole performed on land (Chay-Tumus[28], referred to in Fig. 3); the red circle shows the position of the borehole performed offshore (borehole 1D-11, referred to in Fig. 3). **b**, Seepage intensity and spatial density distribution (shown as different colours and heights) in the study area (see Supplementary Information for description of seep analysis methodology). The vessel track is shown as a brown line.
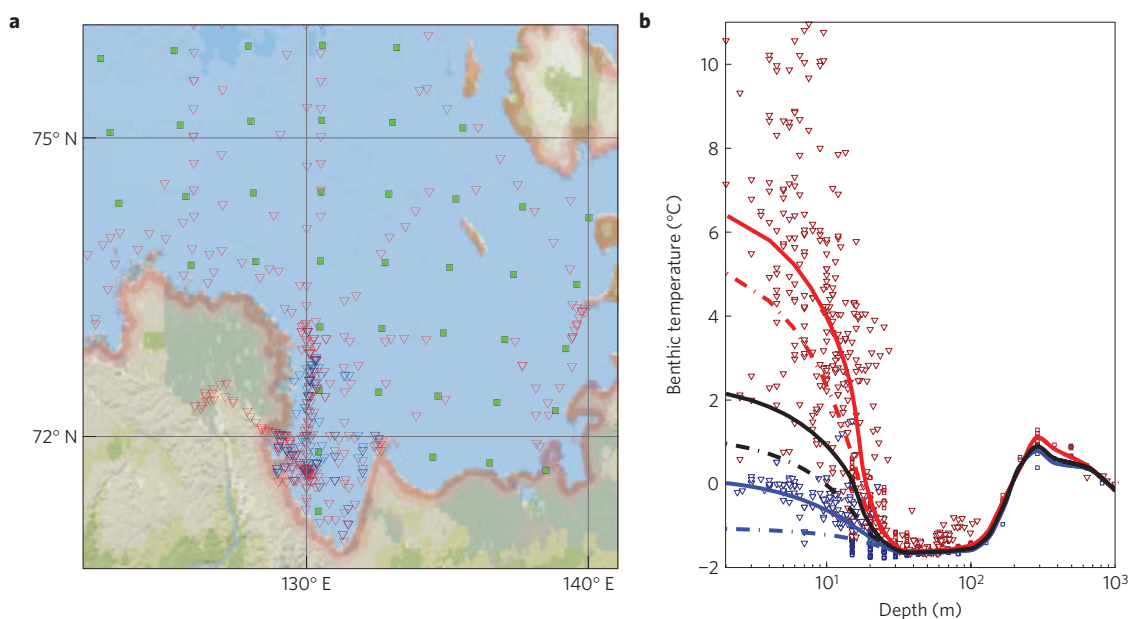

Figure 2 | Dynamics of the bottom water observed in the coastal zone of the ESAS (1999–2012). a, Position of oceanographic stations where the bottom water temperatures observed in summer are marked by red triangles; winter stations are marked by blue triangles; historical data are marked by green squares. **b**, Red and blue triangles represent the measured values of bottom water temperature for each station in **a**. Dashed lines reflect historical data (http://research.iarc.uaf.edu/SSSS); black, annual mean bottom water temperature (MBWT); blue, winter MBWT; red, summer MBWT. Solid lines reflect modern MBWT from the stations marked in **a**: black for annual, blue for winter and red for summer.

One such factor affecting bubble-associated processes is wind-driven air–sea gas exchange[25] during storms, when wind speed increases to $\geq 15\,\mathrm{m\,s^{-1}}$ and the mixed layer thickness increases many times owing to deep water mixing. Such events have the potential to rapidly ventilate bubble-originating/released dissolved CH_4 from the water column, producing high emission rates to the atmosphere. In the ESAS storms occur frequently (up to 70 days annually[26]), causing the mixed layer to extend down to >50 m depth, that is, to the sea bed[27]. Hence, the purpose of this paper is to quantitatively assess bubble-induced CH_4 emissions that result from subsea permafrost degradation in the coastal area and to evaluate the role of storms as a major emission-forcing factor in the shallow ESAS.

To accomplish our goal, we conducted: a multi-year investigation of the thermal regime of sea water and subsea permafrost in the ESAS coastal area; a simulation of the warming effect of sea water on subsea permafrost integrity; an all-season hydro-acoustical and video investigation of bubble plumes in one long-observed hotspot; and seawater and atmospheric CH_4 observations pre- and post-storm.

Field observations were conducted over a shallow study area ($18.4 \times 10^3\,\mathrm{km}^2$) located in the southern Laptev Sea, east of the Lena Delta (Fig. 1). This area was documented as a high-emissions-activity site ('hotspot')[5] serving as a source of CH_4 to the atmosphere using the following criteria: highly elevated concentrations of dissolved CH_4 (compared with levels in the surrounding areas, including upstream in the Lena Delta[6]) observed annually since 2005 (≤ 850 nM in summer and $\leq 3{,}000$ nM in winter[5]); numerous bubbles with very high CH_4 content entrapped in the sea ice observed during the winter[5]; and increased atmospheric CH_4 concentrations documented in the atmospheric boundary layer[5] over the water.

Conductivity–temperature–depth data records of bottom water temperature from more than 570 stations were obtained during summer cruises and winter expeditions performed from 1999 to 2012 (Supplementary Methods). Contrary to the conclusions reached by some authors based on data sets that lacked coverage in the near-shore zone[7,14], our multi-year all-season data show that in the ESAS near-shore zone the mean annual bottom water temperature has increased >0.5 °C during the past fourteen years (1999–2012); in summer this increase reaches >1 °C (Fig. 2).

The thermal state of subsea permafrost in the study area was investigated by drilling down to 57 m below the sea floor from the fast ice in April 2011 (Supplementary Methods and Fig. 1). The temperature of the sediment core extracted from the borehole varied from −1.8 to 0 °C. The surface sediment layer exhibited the lowest temperature of −1.8 °C, but was entirely unfrozen owing to high salt content. Lower sediment layers were also unfrozen despite the low level of mineralization in the sediments. An on-land sediment core obtained from the Chay-Tumus[28] borehole was 8–12 °C colder than that recovered in our study (Fig. 3).

We employed newly obtained data to update the historical data set and to determine the thermodynamic state of sediments over decadal and multi-decadal timescales. Thermal conductivity and the heat capacity of the ground material were parameterized as functions of ice, liquid water, and salt concentration as previously described[13]. The thermodynamic model was forced by seawater temperature dynamics computed by global circulation models (GCMs). As GCMs provide coarse-resolution temperature dynamics, we incorporated local seawater warming effects. The initial temperature distribution was set to measured values collected during drilling. To compute temperature dynamics at sites within tectonic fault zones (Supplementary Fig. 2), we used a two-dimensional realization of the thermodynamic model, which allows the formation and evolution of an open talik to be simulated. The computational domain and heat fluxes at its boundaries were
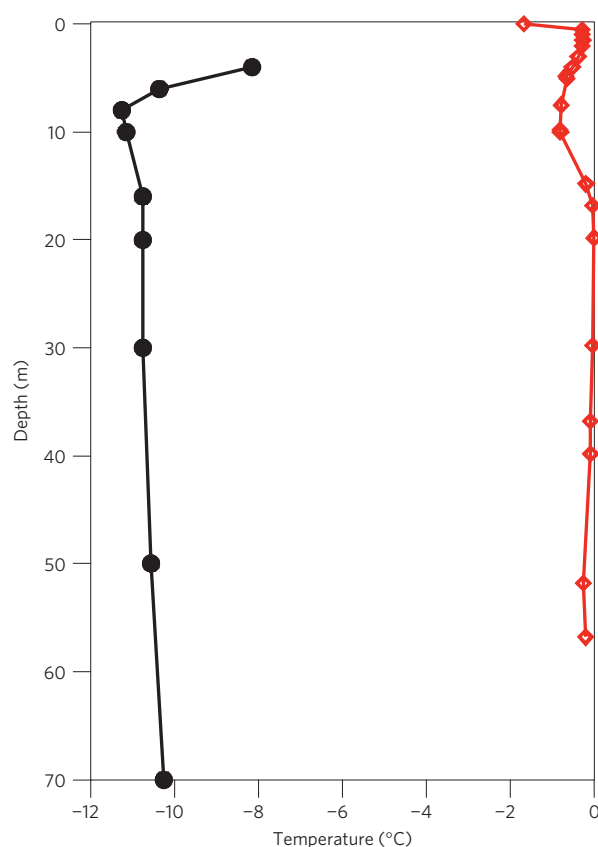

Figure 3 | Difference in thermal regime of terrestrial and subsea permafrost in the coastal zone of the ESAS. The black curve shows the temperature of the sediments at different horizons of the sediment core obtained on land in Chay-Tumus[28] (the position of the borehole is marked by a black circle in Fig. 1a); the red curve shows the temperature of the sediment core obtained offshore in Buor-Khaya Bay (borehole 1D-11; the position of the borehole is marked by a red circle in Fig. 1a). As seen from the temperature curves, sediments in the 1D-11 borehole are much warmer (from −2 to 0 °C) than those from the on-land site (from −8 to −11.5 °C).

determined as previously described[13]. Our results demonstrate that bottom water warming determines the distribution of open taliks in the coastal ESAS area; this distribution correlates well with hotspot areas that exhibit highly elevated aqueous CH_4 concentrations (Fig. 4).

Storm-associated ship-based observations were made in September 2009 and 2010 as part of the International Siberian Shelf Study (ISSS) Program. The first expedition (ISSS-09) departed Tiksi on 25 August 2009. Data were collected starting a few hours post-storm and showed unexpectedly low dissolved CH_4 concentrations (mean 7.7 ± 0.9 nM, 1 s.d.; Fig. 5a), far below previously documented values[5]. Similarly, relatively low atmospheric CH_4 mixing ratios, 1.85–1.97 ppm, mean 1.93 ± 0.07 ppm (1 s.d., Fig. 5c, blue line) were observed, although still above the latitude-specific monthly mean of 1.86 ppm. Repeat measurements performed ∼36 h post-storm showed highly elevated dissolved CH_4 concentrations, comparable to previous observations (Fig. 5b). A corresponding atmospheric CH_4 mixing ratio increase to mean 2.2 ± 0.3 ppm (1 s.d., Fig. 5c, red line) was also observed.

The ISSS-10 cruise departed 24 August 2010 to revisit the study area and to collect repeat observations. On days 1 and 2, wind speeds were 5–8 m s^{-1}, yielding aqueous concentrations of 22.4–800 nM (mean 247.2 ± 18.6 nM, 1 s.d., Fig. 5d). Atmospheric venting under these conditions resulted in atmospheric CH_4 mixing ratios from 1.9 to 3.1 ppm (mean 2.5 ± 0.4 ppm, 1 s.d., Fig. 5f, red line). On
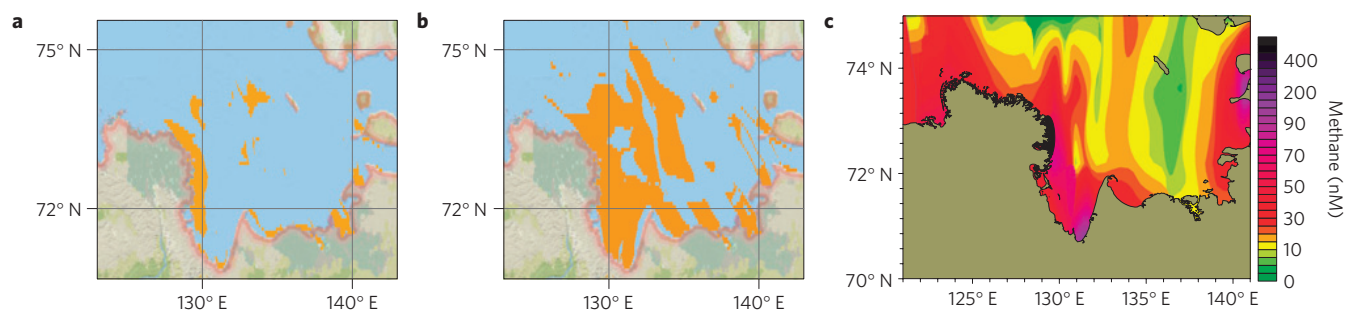
Figure 4 | Simulated areas of open taliks in the coastal area of the ESAS under different thermal regimes of sediments determined by bottom water temperature. a, Areas of taliks based on historical data sets describing bottom water temperatures. **b**, Areas of taliks based on historical data sets updated with modern data (1999–2009). **c**, Areas of methane hotspots observed in the coastal area.
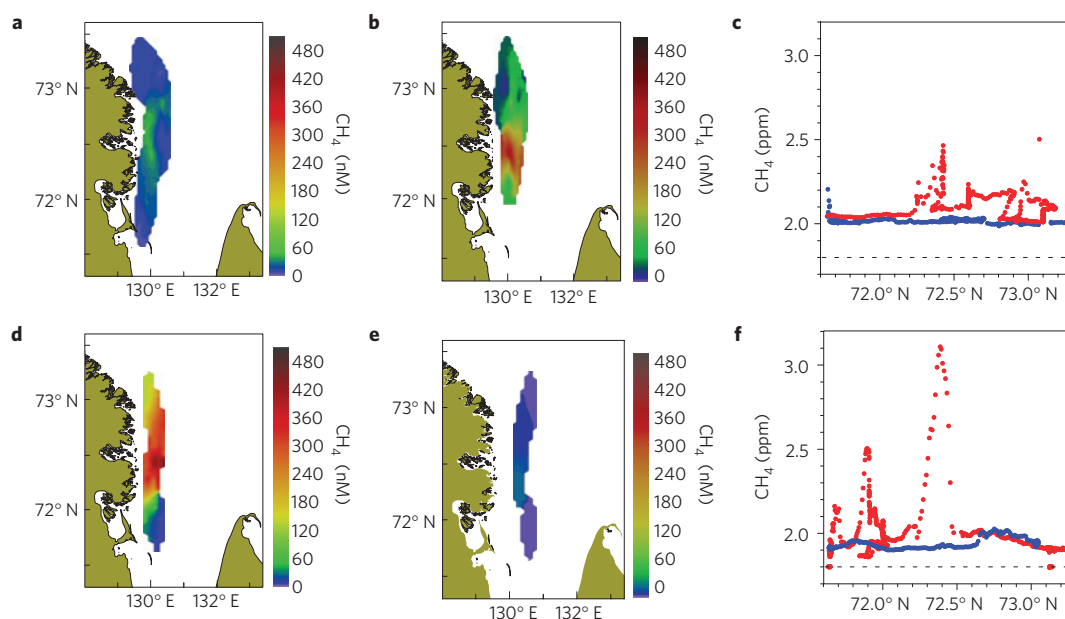

Figure 5 | Pre/post-storm dynamics of aqueous CH$_4$ and atmospheric CH$_4$ mixing ratios. a–f, Observed dynamics during different stages of the storm in 2009 (**a–c**) and 2010 (**d–f**). **a,b**, Water-column CH$_4$ concentrations right after the storm event (**a**; wind speed, U, 2–6 m s^{-1}) and two days after the storm (**b**; $U = 4$–7 m s^{-1}). **c**, Atmospheric CH$_4$ mixing ratios (blue line corresponds to **a**; red line to **b**). **d,e**, Water-column concentrations before and at the beginning of the storm (**d**; U increasing from 5–8 m s^{-1} to $U > 15$ m s^{-1}) and several hours after the storm (**e**; $U = 3$–8 m s^{-1}). **f**, Atmospheric CH$_4$ mixing ratios (the blue line corresponds to **e**; the red line to **d**).

day 3 winds increased to >15 m s^{-1}, forcing operational suspension for safety reasons until a few hours post-storm. By then, dissolved CH$_4$ concentrations had decreased to a mean of 13.8 ± 2.9 nM, 1 s.d. (Fig. 5e) and atmospheric CH$_4$ mixing ratios had decreased correspondingly to a mean of 1.92 ± 0.16 ppm (1 s.d., Fig. 5f, blue line). This second year of field observations confirmed a storm ventilation mechanism, that is, storm-driven water-column and atmospheric boundary layer CH$_4$ reservoir depletion, followed by rapid replenishment; this pointed to an intrinsically strong seabed CH$_4$ source, which could be ebullition.

To assess rates of bubble-induced CH$_4$ fluxes from the study area, an extensive multibeam survey, including a 24-h multibeam sonar lander deployment, was performed in the study area. A 260 kHz 8-bit Imagenex Delta-T multibeam sonar was used for the surveys because of its portability, its durability (no moving parts, sensitive power transformers, or external beam-forming computers), and its ability to be run by a laptop computer. The system continuously recorded water-column returns for all beams during the entire survey; beams were formed both in real time and in post-processing. A laboratory calibration experiment with the Delta-T confirmed a positive correlation

between summed sonar return and bubble plume gas volume (Supplementary Fig. 3). Calibration data were collected by rotating the sonar around a vertical axis in a 5-m-deep tank at a range of 6 m from a flow-controlled air bubble plume. Data were in agreement with previous field measurement data of natural marine hydrocarbon seep bubbles[18,19,29] and with laboratory data[30] and showed that bubble plume appearance in video and multibeam is strongly sensitive to flux.

The area of study was extended further around the Lena Delta to investigate whether ebullition was widespread within the projected talik area. Water-column multibeam sonar data were recorded throughout the survey as pings of raw sonar return for 120 beams with 500 samples per beam regardless of range. Sonar returns were normalized for acquisition gain to facilitate comparison across different data blocks. Sonar data acquisition recorded 157 survey lines of variable duration that were imported from the Imagenex Delta-T data files in intervals of 6,000 sequential pings, hereafter referred to as 'blocks'. A total of 1,178 blocks were created, representing between 100 m and 3,175 m of linear 'along-track' survey distance. The mean length of the blocks was ~1,600 m. Blocks were sub-divided into 200 m along-track intervals termed

Table 1 | Summary of parameters derived from sonar data and used for flux calculation.

Seep intensity class	Fraction (%)	Total seeps (no.)	Bubble radius (μm)	Bubble rate (no. s⁻¹)	Volume per seep (cm³ s⁻¹)	Volume per class (l s⁻¹)	Spatial flux (mg m² d⁻¹)	Total flux from hotspots (Tg y⁻¹)
A. Best estimate								
i1	43	7,873	3,750	3	0.66	5.21	23	1.34
i2	29	5,319	3,750	15	3.31	17.62	78	5.04
i3	25	4,545	3,750	25	5.52	25.09	111	7.20
i4	4.2	769	3,750	100	22.09	16.9	75	4.42
Total	100	18,506				64.92	287	18.0
Mean			3,750	15.9	3.51			
B. Maximum shift of population towards smaller seeps								
i1	32	5,905	3,750	3	0.66	3.91	17	1.02
i2	22	3,989	3,750	15	3.31	13.21	59	6.06
i3	40.5	6,045	3,750	25	5.52	33.38	148	9.25
i3	5.5	1,023	3,750	100	22.09	22.59	100	5.83
Total	100	16,962				73.10	324	22.16
Mean			3,750	17.88	3.35			
C. Maximum shift of population towards larger seeps								
i1	57	10,471	3,750	3	0.66	6.93	31	1.79
i2	22	7,074	3,750	15	3.31	23.43	104	6.08
i3	17.9	3,408	3,750	25	5.52	18.82	83	4.86
i4	3.1	576	3,750	100	22.09	12.74	56	3.29
Total	100	21,531				61.94	274	16.02
Mean			3,750	15.15	3.35			
D. Maximum smaller bubble size								
i1	43	7,873	2,625	3	0.23	1.78	8	0.44
i2	29	5,319	2,625	15	1.14	6.04	27	1.56
i3	23.8	4,545	2,625	25	1.89	8.60	38	2.24
i4	4.2	2,625	2,625	100	7.58	5.82	26	1.5
Total	100	18,506				22.26	99	5.74
Mean			2,625	15.88	1.2			
E. Maximum larger bubble size								
i1	43	7,873	4,875	3	1.46	11.46	51	2.97
i2	28	5,309	4,875	15	7.28	38.71	171	10.01
i3	25	4,545	4,875	25	12.13	55.14	244	14.27
i4	4	760	4,875	100	48.53	37.31	165	9.66
Total	100	18,506				142.64	632	36.91
Mean			4,875	15.88	7.71			

A detailed description of the data acquisition and analysis, and a discussion of the uncertainties associated with the method are presented in Supplementary Sections 1.8, 1.9 and 2.0.

'sub-blocks'; a total of 8,203 sub-blocks were manually inspected and assigned a density class and intensity class.

The survey documented 2.7×10^4 bubble plume seeps along the ~2,000-km-long ship route in 6–24 m water depths (Fig. 1b and Supplementary Fig. 4). These data show bubble plumes extending to near the sea surface (Supplementary Fig. 5). To estimate flux, seeps were classified into one of four intensity classes: short bubble clumps (seep intensity class i1), pulses of bubbles >50% active (i2), thin continuous bubble streams (i3), and thick continuous bubble streams (i4). Seeps observed in the study area were also classified into density classes: spatial density of 2.16×10^3 seeps km^{-2} composed density class 1, 8.56×10^2 seeps km^{-2}: density class 2, 2.9×10^2 seeps km^{-2}: density class 3, and 4.1 seeps km^{-2}: density class 4 (Table 1 and Supplementary Methods and Fig. 4). Owing to the large number of sonar blocks analysed (8,203), the number of seeps in each class is well characterized except for the smallest, where misclassification of noise could lead to an undercount. Uncertainty in the flux assignment for each intensity class was addressed by estimating maximum likely limits that the flux classification probability could be biased towards larger or smaller classes or that the dominant bubble size could be different, while still maintaining the same bubble plume appearance (Table 1 and Supplementary Figs 6 and 7). Combining estimated seep intensity and density class emission rates yields a conservative best estimate of 290 mg m^{-2} d^{-1} ebullition-induced flux (ranging from 100 to 630 mg m^{-2} d^{-1}; see below). This mean flux is >10 times greater than was previously suggested for the ESAS hotspots[5].

The largest uncertainty of our estimates is related to bubble size and temporal variability of fluxes. To address uncertainties related to bubble size, a range of estimates was made for probability shifts (±25%) favouring smaller and larger plumes, yielding emissions of 325 and 275 mg m^{-2} d^{-1}, respectively (Table 1). Thus, the

calculation is insensitive to the underestimation of large plume occurrence, but is sensitive to the small plume occurrence, because small plumes were far more numerous. If representative bubble plume bubbles were 30% smaller (2,625 μm diameter), emissions decreased to 100 mg m^{-2} d^{-1}; if 30% larger (4,875 μm diameter), emissions increased to 630 mg m^{-2} d^{-1}. The average of these four limits and the best-guess estimate is 290 mg m^{-2} d^{-1}. Note that this average was derived on the basis of the entire data set obtained, not only within the study area, but also outside it along the 2,000 km ship track. In addition, in our estimates we assume that bubbles are released only 50% of the time, whereas only one of four seep classes releases bubbles so infrequently. This underscores the fact that our release estimates are definitely conservative. Uncertainties related to spatial and temporal variability of fluxes remain.

Present observations provide an opportunity to constrain the bubble-induced CH$_4$ flux from shallow ESAS hotspots. Extending the best summer ebullition-induced flux estimation of 290 mg m^{-2} d^{-1} to the studied hotspot area of 18.4×10^3 km^2 and assuming that ebullition occurs only 50% of the time yields a conservative annual flux estimate of 0.9 Tg CH$_4$ for this hotspot area. Hotspot areas were apportioned on the basis of two complementary approaches: a statistical approach (using an empirical distribution function test) and a geological approach (considering areas of fault zones in the ESAS, Supplementary Fig. 2); both approaches have been described in detail previously[5]. Given that the study area covers ∼10% of the ESAS hotspots[5], storm- and bubble-induced CH$_4$ release from ESAS hotspots to the atmosphere is estimated at 9 Tg CH$_4$ annually (Table 1), increasing our estimate of total ESAS CH$_4$ emissions to atmosphere to 17 Tg yr^{-1}.

These are conservative estimates. Specifically, in our estimates we assume that bubbles are released only 50% of the time, a rate that was accurate for only one of four seep classes (i1); the remaining classes i2–i4 emitted bubbles more than 50% of the time. Moreover, in our previous assessment, 'hotspots' were defined and their area apportioned exclusively by increased aqueous CH$_4$ in the surface water layer[5] but in fact highly elevated CH$_4$ concentrations (up to 900 nM) have been observed in the sub-surface layer just below the pycnocline (10–20 m deep) over extensive ESAS areas[6].

The coastal area permafrost is still thought to be the most stable in the ESAS (refs 14,15); however, our data show that coastal subsea permafrost is being degraded, forming migration pathways for seabed gaseous CH$_4$ and increasing the role of bubble-induced fluxes in annual atmospheric emissions from the ESAS. As >75% of the total ESAS area is <50 m in depth, the water column provides bubbles with a very short conduit to the atmosphere. Storms enable more CH$_4$ release because they destroy shallow water stratification and the mixed layer thickness increases many times owing to deep water mixing, thus increasing gas exchange across phase boundaries. As a result, bubble-mediated, storm-induced CH$_4$ 'pulses' force a greater fraction of CH$_4$ to bypass aqueous microbial 'filters' and reach the atmosphere. These results have important implications for CH$_4$ atmospheric emissions from all Arctic seas that are underlain with subsea permafrost. Increasing storminess[31–33] and rapid sea-ice retreat[34–36] causing increased CH$_4$ fluxes from the ESAS are possible new climate-change-driven processes. Continuing warming of the Arctic Ocean[9,37,38] will strengthen these processes.

Methods

Water samples were collected and analysed, and results statistically tested as described previously[5]. CH$_4$ concentrations were measured with a pre-calibrated (by manufacturer) high-accuracy fast CH$_4$ analyser (HAFMA, DLT-100; response time: <0.05 s; accuracy: better than 1% of reading; concentration range: 0.01–25 ppmv; www.lgrinc.com). Seawater temperature measurements were performed using a pre-calibrated shipboard conductivity–temperature–depth sond attached to a large metal rosette wheel. A heavy drilling technique was used for drilling the subsea permafrost in the study area in April 2011. Temperature in the borehole

was measured 3 days after drilling using a chain of calibrated thermistors, according to the Global Terrestrial Network for Permafrost (GTN-P) protocol (http://www.gtnp.org). A modification of the permafrost model described in ref. 13 was performed as a case study. The thermodynamic model was forced by seawater temperature dynamics computed by GCM. The initial temperature distribution was set to values measured during drilling. To compute temperature dynamics at sites within tectonics fault zones we used a two-dimensional realization of the thermodynamic model, which allows the formation and evolution of an open talik to be simulated. The computational domain and heat fluxes at its boundaries were determined as described in ref. 13. To assess CH$_4$ ebullition fluxes, we analysed sonar data obtained with a 260 kHz 8-bit Imagenex Delta-T multibeam sonar (Supplementary Methods). The system continuously recorded water-column returns for all beams during the entire survey. The Delta-T produces 120 across-track beams by a 3° along-track swath; beams were formed in real time and in post-processing. Sonar returns were normalized for acquisition gain to facilitate comparison across different data blocks. Sub-blocks were filtered for erroneous pings and processed in radius-theta (beam angle) space. Each data block was classified for two characteristics: spatial density, d, and seep intensity, i. The probability of each class was determined for each data block. Emission rates were then normalized to per square metre values based on each segment's along-track distance and swath width. Full methodology details are in the Supplementary Methods.

References

1. Solomon, S. D. (ed.) *Climate Change 2007: The Physical Science Basis* (Cambridge Univ. Press, 2007).
2. Friedlingstein, P. *et al.* Climate-carbon cycle feedback analysis: Result from the C^{4}MIP model intercomparison. *J. Clim.* **19,** 3337–3353 (2006).
3. Gruber, N. *et al.* in *The Global Carbon Cycle: Integrating Humans, Climate and the Natural World* (eds Field, C. B. & Raupach, M. R.) 45–76 (Island Press, 2004).
4. Vonk, J. E. *et al.* Activation of old carbon by erosion of coastal and subsea permafrost in Arctic Siberia. *Nature* **489,** 137–140 (2012).
5. Shakhova, N. *et al.* Extensive methane venting to the atmosphere from the sediments of the East Siberian Arctic Shelf. *Science* **327,** 1246–1250 (2010).
6. Shakhova, N. *et al.* Geochemical and geophysical evidence of methane release from the inner East Siberian Shelf. *J. Geophys. Res.* **115,** C08007 (2010).
7. Biastoch, A. *et al.* Rising Arctic Ocean temperatures cause gas hydrate destabilization and ocean acidification. *Geophys. Res. Lett.* **38,** L08602 (2011).
8. Holemann, J. *et al.* Near-bottom water warming in the Laptev Sea in response to atmospheric sea-ice conditions in 2007. *Polar Res.* **30,** 6425–6440 (2011).
9. Serreze, M. & Barry, R. Processes and impacts of Arctic amplification. *Glob. Planet. Change* **77,** 85–96 (2011).
10. Soloviev, V. A., Ginzburg, G. D., Telepnev, E. V. & Mikhaluk, Yu. N. *Cryothermia and Gas Hydrates in the Arctic Ocean* (Sevmorgeologia, 1987).
11. Romanovskii, N. N., Hubberten, H-W., Gavrilov, A., Eliseeva, A. & Walker, D. Offshore permafrost and gas hydrate stability zone on the shelf of East Siberian seas. *Geo-Mar. Lett.* **25,** 167–182 (2005).
12. Nicolsky, D. & Shakhova, N. Modeling sub-sea permafrost in the East Siberian Arctic Shelf: The Dmitry Laptev Strait. *Environ. Res. Lett.* **5,** 015006 (2010).
13. Nicolsky, D. J. *et al.* Modeling subsea permafrost in the East Siberian Arctic Shelf: The Laptev Sea region. *J. Geophys. Res.* **117,** F03028 (2012).
14. Dmitrienko, I. A. *et al.* Recent changes in shelf hydrography in the Siberian Arctic: Potential for subsea permafrost instability. *J. Geophys. Res.* **116,** C10027 (2011).
15. Romanovskii, N. N. & Hubberten, H-W. Results of permafrost modeling of the lowlands and shelf of the Laptev Sea region, Russia. *Periglac. Process.* **12,** 191–202 (2001).
16. Shakhova, N., Nicolsky, D. & Semiletov, I. Current state of sub-sea permafrost on the East-Siberian Shelf: Testing of modeling results by observational data. *Dokl. Earth Sci.* **429,** 1518–1521 (2009).
17. Leifer, I. & Patro, R. The bubble mechanism for transport of methane from the shallow seabed to the surface: A review and sensitivity study. *Cont. Shelf Res.* **22,** 2409–2428 (2002).
18. Leifer, I. Characteristics and scaling of bubble plumes from marine hydrocarbon seepage in the Coal Oil Point seep field. *J. Geophys. Res.* **115,** C11014 (2010).
19. Leifer, I., Luyendyk, B. P., Boles, J. & Clark, J. F. Natural marine seepage blowout: Contribution to atmospheric methane. *Glob. Biogeochem. Cycles* **20,** GB3008 (2006).
20. Solomon, E. A., Kastner, M., MacDonald, I. R. & Leifer, I. Considerable methane fluxes to the atmosphere from hydrocarbon seeps in the Gulf of Mexico. *Nature Geosci.* **2,** 561–565 (2009).
21. Reeburgh, W. S. Oceanic methane biogeochemistry. *Chem. Rev.* **107,** 486–513 (2007).

22. Greinert, J., McGinnis, D. F., Naudts, L., Linke, P. & De Batist, M. Atmospheric methane flux from bubbling seeps: Spatially extrapolated quantification from a Black Sea shelf area. *J. Geophys. Res.* **115,** C01002 (2010).

23. McGinnis, D. F., Greinert, J., Artemov, Y., Beaubien, S. E. & Wuest, A. Fate of rising bubbles in stratified waters: How much methane reaches the atmosphere?. *J. Geophys. Res.* **111,** C09007 (2006).

24. Greinert, J. & Nutzel, B. Hydroacoustic experiments to establish a method for the determination of methane bubble fluxes at cold seeps. *Geo-Mar. Lett.* **24,** 75–85 (2004).

25. Wanninkhof, R. Relationship between wind speed and gas exchange over the ocean. *J. Geophys. Res.* **97,** 7373–7382 (1992).

26. Proshutinsky, A., Proshutinsky, T. & Weingartner, T. *Northern Sea Route Reconnaissance Report: Climatology of Environmental Conditions Affecting Commercial Navigation along the Northern Sea Route* 148 (Univ. Alaska Fairbanks, Institute of Marine Science, 1994).

27. Nikiforov, E. G. & Shpaikher, A. O. *Features of the Formation of Hydrological Regime Large-Scale Variations in the Arctic Ocean* (Hydrometeoizdat, 1980).

28. Grigoriev, N. F. *Mnogoletnemerzlie porodi primorskoy zoni Yakutii* (Nauka, 1986).

29. Leifer, I. & Boles, J. Turbine seep-tent measurements of marine hydrocarbon seep forcing on sub-hourly time scales. *J. Geophys. Res.* **110,** C01006 (2005).

30. Leifer, I. & Culling, D. Formation of seep bubble plumes in the Coal Oil Point seep field. *Geo-Mar. Lett.* **30,** 339–353 (2010).

31. Groisman, P. & Soja, A. J. Ongoing climatic change in Northern Eurasia: Justification for expedient research. *Environ. Res. Lett.* **4,** 045002 (2009).

32. Francis, O. P., Panteleev, G. G. & Atkinson, D. E. Ocean wave conditions in the Chukchi Sea from satellite and *in situ* observations. *Geophys. Res. Lett.* **38,** L24610 (2011).

33. Sepp, M. & Jaangus, J. Changes in the activity and tracks of Arctic cyclones. *Clim. Change* **105,** 577–595 (2011).

34. Notz, D. The future of ice sheets and sea ice: Between reversible retreat and unstoppable loss. *Proc. Natl Acad. Sci. USA* **106,** 20590–20595 (2009).

35. Wadhams, P. Arctic ice cover, ice thickness and tipping points. *Ambio* **41,** 23–33 (2012).

36. Parmentier, F-J. W. *et al.* The impact of lower sea-ice extent on Arctic greenhouse-gas exchange. *Nature Clim. Change* **3,** 195–202 (2013).

37. Screen, J. A. & Simmonds, I. The central role of diminishing sea ice in recent Arctic temperature amplification. *Nature* **464,** 1334–1337 (2010).

38. Richter-Menge, J. & Overland, J. E. *Arctic Report Card* http://www.arctic.noaa.gov/reportcard (2010).

Author contributions

N.S., I.S., I.L. and V.S. designed the field work; A.S. and D.K. collected the water samples, set up the analytical instruments, performed the onboard measurements, and conducted quality control; C.S. collected and analysed sonar data; N.S., I.S., A.S., D.N. and I.L. analysed the data; N.S., D.K., D.N., I.L., and A.S. created the figures; N.S., I.S., I.L., and O.G. drafted the first manuscript; and all authors contributed to the final version.